

A Multi-Material 3D Printing-Assisted Micropatterning

Sayli Jambhulkar

Arizona State University

Dharneedar Ravichandran

Arizona State University

Varunkumar Thippanna

Arizona State University

Dhanush Patil

Arizona State University

Kenan Song (≥ kenan.song@asu.edu)

Arizona State University

Research Article

Keywords: 3D Printing, Multiphase Direct Ink Writing, micropatterning, microfluidic, wet etching, heat-dissipation

Posted Date: March 7th, 2023

DOI: https://doi.org/10.21203/rs.3.rs-2592362/v1

License: © (1) This work is licensed under a Creative Commons Attribution 4.0 International License.

Read Full License

Abstract

Micropatterned structures have applications in microchips, circuit board designs, microfluidics, evaporator/condenser coils, microelectronics, metasurfaces, and other functional devices. Conventional microfabrication techniques include lithography, vapor deposition, and laser writing. However, these methods have slow processing rates, complex requirements, or costly procedures. As a result, it is challenging to fabricate micropatterned structures onto large-scale surfaces with high production rates and resolution features. Thus, this study focuses on a non-conventional, mask-free micropatterning technique that combines bottom-up 3D printing capable of processing multiple materials and top-down wet etching for selective elimination of sacrificial material. The unique 3D printing, Multiphase Direct Ink Writing (MDIW), utilizes various polymer and nanoparticle systems as feedstocks for depositing lamellar structures containing sublayers of varying compositions (i.e., wet etchable sacrificial ink and ultravioletcurable patterning ink). The rapid phase transformation of photosensitive ink into solidified features enables "micro-confinement" of the sacrificial ink. Subsequently, wet etching can locally and selectively dissolve sacrificial polymers by solvent diffusion and polymer dissolution at the polymer-solvent interface. The parameter control (i.e., ink rheology, polymer-polymer interdiffusion, layer multiplication, phase transformation, and solvent-polymer interactions) can precisely tune the lamellar-groove transition, thus forming desirable surfaces or internal microstructures. Our MDIW 3D printing and its facilitation in surface micropatterning demonstrate the massive potential of distributing nanoparticles for dissipating thermal energies. With production scalability, operation simplicity, and multi-material compatibility, our 3D-printed micropatterning shows broader applications in nanoparticle assembly, drug delivery, optical lenses, intelligent microbots, and morphing objects.

1 Introduction

Surface patterned 2D or 3D microstructures (*e.g.*, dots, lines, grooves, wells, sieves, pillars, and cellular solids) have been of significant importance in numerous applications, such as microfluidics, microelectronics, optoelectronics, photovoltaics, microreactors, and biomedical devices.[1–6] Conventional techniques used to generate micropatterned surfaces include self-assembly (*e.g.*, coffee ring, flow field, electrical field, or magnetic field directed assembly), micromolding (*e.g.*, roll-to-roll, microcontact printing, replica molding, solvent-assisted micromolding), lithography (*e.g.*, soft lithography, electron beam lithography, nanoimprint lithography), and vapor deposition (*i.e.*, physical vapor deposition (PVD), chemical vapor deposition (CVD)).[7–12] Among these techniques, self-assembly has been effective in nanomaterial organizations. However, the thermodynamically and kinetically controlled procedure often appears in small-area or volume fabrications.[13] For example, block-copolymer (BCP) crystals can be engineered with pre-designed surfaces that nanoparticles can form orientations or periodicity with external field stimuli.[7, 14] In comparison, micromolding has acceptable scalability due to its simple mechanism but only provides 2D surface features.[15] On the contrary, lithography-based methods can design complex features but have tedious multistep processes (*e.g.*, spin coating, masking, baking, developing, and etching) with delicate parameter control.[16] Vapor deposition techniques can

generate submicron to nanoscale featured resolutions; however, the high pressure and temperature-controlled reactions are slow and chemically complex, with large footprint apparatuses in scalable manufacturing.[10]

Etching for fabricating micro or nanoscale features is essential in semiconductor industries.[17] Dry etching methods avoid chemical solvents and can provide high processing precisions, but they are limited to a few costly techniques, *e.g.*, reactive ion etching, plasma etching, and multiphoton lithography. [18] Comparatively, wet etching is a cost-efficient and convenient technique for delicate structural design, primarily *via* polymer-assisted patterning and selective elimination.[19] For example, in microlithography, polymer dissolution plays a crucial role in fabricating positive and negative resist for the semiconductor industry. Another example is inkjet-etching, which can fabricate concave surface microstructures, such as microwells and microgrooves, by ejecting organic solvent droplets onto an insulator polymer film, followed by polymer dissolution.[20, 21] However, the polymer dissolution strategy only generates as high feature resolutions as hundreds of microns, with limited microfeature depth up to the sub-micrometer range.[22] The universal etching rates from the solvent-polymer interactions also affect the patterning regularity. Moreover, selective etching of uniform surfaces may need mask assistance, adding time and technical challenges to patterning processing. Hence, it is still challenging to fabricate surface micropatterning with controlled high-resolution or tunable morphology in a low-cost, large-area, highly efficient, and flexible way.

As an alternative to conventional micropatterning approaches, 3D printing has played an essential role in micropatterning. Via 3D printing, small molecules and nanoparticles can be assembled through an ondemand manufacturing and maskless process. Different 3D printing approaches, such as stereolithography (SLA),[23-25] digital light processing (DLP),[26] volumetric printing,[27] continuous liquid interface production (CLIP),[6, 28] fused deposition modeling (FDM),[29] direct laser writing (DLW), [30] direct ink writing (DIW),[31] electrohydrodynamic jetting (EHD),[32, 33] aerosol jet,[34] and inkjet,[20, 35] have been studied for regular or irregular patterns, hierarchies, or architectures via a layer-by-layer additive strategy. Many of these 3D printing techniques have proven a high degree of design flexibility to fabricate functional devices, such as origami structures, heat exchangers, circuit boards, batteries, supercapacitors, sensors, actuators, microfluidic devices, and biomedical devices. [36, 37] However, photosensitive monomer-based printing (e.g., SLA, DLP, CLIP, DLW) relies on a limited class of monomers with residue on printed objects mandating the post-processability.[38] Current extrusion-based methods (e.g., FDM, DIW) can print various topologies but also have difficulties printing multiple materials, manipulating sub-printing line compositions, or designing submicron structures. Ink-based methods (e.g., EHD, aerosol, and inkjet) have been the mainstream in printed circuit boards due to their high-resolution control at the micron or even nanoscale; however, the printing speed has been limited to the nozzle size and ink quality, especially at the microscale.

This paper reports the facile and mask-free technique for fabricating micropatterns by combining bottomup 3D printing and top-down wet etching methods. A 3D printing platform, Multiphase Direct Ink Writing (MDIW), has been developed for the first time with multi-material compatibility and wet etchability for micropattern fabrication. The MDIW 3D printing has two immiscible, solvent-free inks printed into lamellar structures. These two inks consist of alternating sublayers of wet-etchable sacrificial ink (*i.e.*, polyethyleneimine (PEI)) and UV-curable patterning ink (*i.e.*, epoxy (E) and boron nitride nanoparticles (BNs)). The 3D-printed multilayer structures show varying morphology and resolution that can be manipulated via polymer-polymer phase separations, ink rheology, layer multiplications, and phase transformation. The phase transformation of UV-curable ink forms patterning sublayers (PLs) with microconfined inks for the sacrificial sublayers (SLs). These SLs are removable during the selective polymer dissolution process, leading to micropatterns (*i.e.*, arrays of microgrooves) tunable via polymer-solvent interaction thermodynamics/kinetics. These micropatterns contain the anisotropic distribution of thermally conductive BNs and confined coolants that form thermally conductive pathways to dissipate heat. This layer additive essence via our MDIW also suggests the merits of processing scalability (≈ 7.35 cm²/hr) and material flexibility, creating functional morphologies or architectures more quickly and cost-efficiently compared to conventional mask-assisted or vapor-deposited protocols.

2 Experimental Section

2.1 Materials

Polyethyleneimine with branched molecular structure (molecular weight M_w 25,000, density, 1.05 g/ml, CAS number 25987-06-8) was purchased from Sigma-Aldrich, USA. The transparent acrylic epoxy (Loctite AA3494, product number 235070) was purchased from Krayden, Inc., USA. Boron nitride (BN) nanoparticles (500 nm) (99.5%, product number 1523DX) were purchased from Sky Spring Nanomaterials Inc., USA. Ethanol (ACS reagent, 99.5%, CAS number, 64-17-5) and IPA (ACS reagents, natural, \geq 98%, FG, CAS number, 67-63-0) were purchased from Sigma-Aldrich, USA.

2.2 3D Printing Ink Preparations

The BN nanoparticles were added to the 50 ml of epoxy at different concentrations (5–30 wt.%) to obtain the composite ink as surface patterning (PL) compositions (Table 1). Next, the BNs were added to epoxy while the mixture was mechanically stirred for 2 hr until uniform mixing was obtained. After that, the prepared mixture was evacuated at room temperature for 24 hr to remove bubbles before 3D printing. Lastly, 50 ml of PEI was heated at 50°C inside an oven (model of Lindberg Blue M from Thermo Scientific) as SL material for printing.

Table 1 Ink compositions and sample nomenclature.

Feedstocks	Polymer	BN (wt.%)	Nomenclature
UV-curable patterning layer (PL) material	Ероху	0	E
		5	E-BN5
		10	E-BN10
		20	E-BN20
		25	E-BN25*
		30	E-BN30
Micropatterned surface with water as a coolant trapped between microchannels for thermal management demonstrations	Ероху	25	E-BN25C
Non-patterned/planar composite surface as the contrast sample	Ероху	25	E-BN25P
Wet etchable sacrificial layer (SL) material to facilitate surface patterning formation	Polyethyleneimine	0	PEI
Sacrificial material heated at different temperatures of X °C	Polyethyleneimine	0	PEI-X^

^{*}E-BN25, 25wt.% BN was selected as the optimized loading due to the printability; ^PEI-50, sacrificial material heated at a temperature of 50°C.

2.3 MDIW 3D Printing

3D printable inks form multilayered lamellar structures *via* a custom-made 3D printing platform. This 3D printer, MDIW, was in-house developed, consisting of a spinneret, a reducer, a minimizer, and several layer multipliers. The design principles detailed in Fig. 1a were modified from our previous publications.[39–41] The printer components were fabricated *via* a metal 3D printer, Concept Laser M2 (GE additive), with metallic powders of Inconel 718 to be mechanically robust and corrosion-resistant during printing. The E-BN25 and PEI heated at a temperature of 50°C (PEI-T50, Table 1) for matching fluid dynamics were loaded into separated stainless-steel syringes and dispensed using syringe pumps (KDS LEGATO 200) at the same flow rate of 1.5 ml/min. Printing paths were guided by computer-aided design (CAD) before being converted into G-code programs by commercial software to control the XYZ motion of the print head. The multilayer structure of E-BN25 and PEI was printed on the glass substrate for all experiments unless otherwise noted. The printed E-BN25 ink was *in situ* crosslinkable while printing on the glass substrate under a UV lamp (*i.e.*, 395–405 nm wavelength). After 3D printing, the printed layered structures were cured within a DYMAX ECE 5000 UV oven (*e.g.*, 325–395 nm) for 30 sec for full solidification. The complete crosslinking networks adhesive to the substrate were critical to avoid structural disruptions (as

seen in **Fig. S1**) during subsequent wet etching. The generated G-code and syringe pump controlled other printing parameters (*e.g.*, print speeds, printing directions, print gap) for optimized patterning structures.

2.4 Wet Etching

The ethanol, water, and isopropyl alcohol (IPA), as good PEI solvents, were used as etchants. The 3D printed samples were immersed in a bath full of an etchant at different etching temperatures of 25 and 35°C while the bath was magnetically stirred at 100 rpm for different durations of 1, 5, 10, 15, and 20 min. When taken out from the etchant bath, these samples were thoroughly rinsed with the respective etchant and dried on the hot plate (Thermo Scientific) at 50°C for 30 minutes before the subsequent etching cycle. After the solvent evaporation, the weight of the sample was measured by Mettler Toledo microbalance as a function of different etching durations, temperatures, cycles, and etchant types to calculate the dissolution of PEI and estimate etching kinetics.

2.5 Material Characterizations

The rheology of E-BN25 and PEI inks was performed using a Discovery HR2 rheometer (TA Instruments) with a 40 mm 2° cone Peltier plate with a 100 µm truncation gap. The viscosity of the samples was measured by flow sweep test from 0.001 to 5000 1/s shear rate. The viscoelastic properties (loss, elastic modulus, and tan delta) were measured by amplitude sweep test from 0.1 to 10000 Pa shear stress at a constant frequency step of 1 Hz. The test geometry temperate was kept at 25°C for E-BN25 ink while the test temperature varied from 25 to 50°C for PEI. The photo-rheology of the sample was tested by irradiating the surface with UV light for 10s, followed by amplitude sweep tests. Thixotropic viscosities were measured at a low shear rate of 0.1 1/s and a high shear rate of 5, 10, 25, and 50 1/s.

The scanning electron microscope (SEM) images, elemental distribution spectroscopy (EDS) mapping, and line profile were taken by a field emission scanning electron microscope (FESEM), operated at 20kV with Auriga SEM/FIB (Zeiss). Before imaging, the sample surface was sputter coated with a thin layer of gold. X-ray diffraction (XRD) spectra were obtained from a PAN analytical X'Pert PRO powder diffractometer in the range of 10 – 70° (20). The optical image, 3D surface imaging, and surface roughness of the multilayer structures were taken from the Keyence VR-3200 3D optical scanning microscope. The cross-sectional imaging of the multilayer structures was performed with the OLYMPUS MX-50 optical microscope. The thermal characteristics of the inks were investigated with a thermogravimetric analyzer (TGA) (TA instruments, TGA 550) and differential scanning calorimetry (DSC) (TA instruments, DSC 250).

The thermal conductivity and thermal diffusivity of the samples was measured with the hot disk TPS-2500S. The through-plane thermal properties were characterized to investigate the effect of composite patterning on the thermal dissipation properties, especially the effects from selective distribution and coolants. The samples with different < 32>, < 64>, and < 128 > layers having identical width (*i.e.*, 10 mm), length (*i.e.*, 10 mm), and average thickness (*i.e.*, 350 μ m) were heated from 20 to 100°C on dynamic mechanical analyzer (DMA) Peltier plate (TA instruments). The surface temperature was recorded with the KEITHLEY digital multimeter (DMM7510). Thermal images were captured *via* an infrared camera E8-

XT (FLIR) with a 320×240-pixel resolution to analyze the thermal conduction and temperature mapping. Also, to demonstrate the heat dissipation effect of the patterned E-BN25 surfaces depending on the strong convection systems, the thermal images were recorded after heating the sample from 20 to 100°C at a 10°C/min heating rate in the presence of air and trapped water, respectively, on < 32 > layered samples.

3 Results And Discussion

3.1 Overview of the Micropatterning Mechanism

Figure 1 shows the micropatterning mechanism *via* the MDIW 3D printing and wet etching procedures. The MDIW 3D printing platform was in-house developed (Fig. 1a) and synchronously connected with the necessary systems, namely: (i) the transitional control over the printing path via G-codes, (ii) the feedstock delivery system via separate syringes and syringe pumps, (iii) the patterning system via the unique printhead, (iv) the in situ curing system via a platform-mounted UV source, and (v) the wet etching system within a chemical-filled bath. Among these components, the most critical part was the design of the printhead consisting of a spinneret, a minimizer, a series of multipliers, and a reducer. The MDIW 3D printing was used for fabricating lamellar structures with alternating sublayers of two polymer inks through a sequential layer multiplication process. Once the polymer inks entered different spinneret channels, the minimizer would reduce the flow area for the potential benefits of increasing shear rates, aligning polymer chains/nanoparticles, and maximizing the printing resolution.[31, 41-43] The initial two polymer inks forming two-layer structures in the spinneret would flow through the several layer multipliers, producing from tens to hundreds of individual sublayers within a single printing line. In each layer multipliers, the polymer ink was cut horizontally into two parts, where one part flew and spread into the top channel, and the other part flew and spread into a bottom channel, followed by stacking (Fig. 1a₁). Through this process of splitting, spreading, and stacking, the layer number was doubled by each multiplier. As a result of 2 inks, one multiplier would produce 4 sublayers, 2 multipliers generate 8 sublayers, and n multipliers lead to 2^{n+1} sublayers within one printing line exiting the reducer. The reducer dimension (e.g., width, thickness) and shape (e.g., circular, rectangular, triangular, trapezium) were programmable. In this study, the rectangular cross-section was to circumvent voids frequently seen in FDM or DIW 3D printing methods. [44, 45] This research has demonstrated layer numbers < n > from < 32 > to < 128>, with a much higher printing speed of \approx 16 mm/s than the current state of the art in similarresolution DIW (Table S1). Note that our in-house MDIW has been first reported for printing composites as structural supports and stimuli-responsive microbots.[39, 46] This study is the novel use of MDIW for micropatterning with standard protocols of 3D printing lamellar structure, phase transformation, and selective wet etching for heat dissipation applications, as demonstrated in Fig. 1.

Interdiffusion of inks is a critical issue in multilayer 3D printing because it can cause interfacial distortion, nonuniform layer width, irregular interface, and nonuniform structural thickness. Therefore, to optimize the layer structure, two immiscible inks with distinct chemical compositions and physical morphology

were coextruded for multilayer 3D printing. The two feedstock inks (i.e., PEI as the wet etchable sacrificial sublayers (SL) vs. epoxy-boron nitride (E-BN) composites as the UV-curable patterning sublayers (PL), Table 1) were used mainly because of the following reasons. (i) The solvent-free inks (PL and SL) provides flexibility of rheology control for 3D printing processibility and uniform layer formability without interfacial diffusion (Fig. 1b₁); (ii) the rapid phase transformation of PL allows little time for interfacial instabilities and facilitates fine-resolution lamellar structure formation (Fig. 1b₂); (iii) the photocrosslinked PL forms strong adhesion to the substrate (e.g., metal, glass, or plastics), which is essential to retain layers integrity while retaining the mechanical, thermal, and chemical properties when exposed to harsh chemical after wet-etching; (iv) the poor adhesion of SL to the printing substrate guarantees stable etching without damaging the multilayer structure (surface tension ≈ 70 mN/m for PL and 31.1– 28.9 mN/m for SL) and avoids wetting from printing materials;[47-49] (v) the hydrophilic SL enables increased etchability upon etchant exposure (e.g., isopropyl alcohol (IPA), ethanol, and water) that could facilitate etching kinetics for precise patterning (Fig. 1b₃);[50, 51] and (vi) highly loaded BNs in patterning materials enhances heat dissipation for microelectronics applications (Fig. 1b₄).[52, 53] The understanding of the ink printability, etched surface morphologies, and thermal conductive properties would establish the processing-structure-property relationships for 3D printed micropatterns.

The hybrid chemical and physical properties enable the creation of lamellar microstructure consisting of sublayers of (i) crosslinkable, non-dissolvable PL and (ii) hydrophilic-dissolvable SL, which is a prerequisite for the successful wet etching process. When the lamellar structure is introduced to a good solvent for the SL (not for the PL due to its crosslinking characteristics), the distinct physio-chemical properties would cause selective removal of SL, creating the micropatterns (*i.e.*, microgrooves) after etching. Theoretically, wet etching is a process of polymer dissolution into a solvent that involves a two-step process consisting of (i) solvent diffusion to induce swelling of the polymer network, allowing increased solute mobility, and (ii) chain disentanglement of swollen polymers for dissolution.[54, 55] Fig. 1c shows the microstructural distribution at the polymer/solvent interface consisting of different segments (*i.e.*, interdiffusion, polymer swelling, and dissolution). The increased mobility of solute would diffuse polymer chains into the surrounding solvent during the wet etching process.[55] The external parameters, such as temperature and agitation, facilitate the polymer dissolution by diffusing etchant molecules and desorbing polymer chains from the swollen polymer gel layer *via* microforces (*i.e.*, van der Waals, centrifugal, and gravitational).[55]

3.2 Ink Rheology and 3D Printing Processibility

3D printing of composite inks is significantly influenced by their rheological properties, such as viscosity, fluid behavior, thixotropic, and viscoelastic properties.[56, 57] The expected goals for the MDIW 3D printing of inks include (i) multilayer formation without any interfacial defects (for PL and SL), (ii) reduction of sublayer width to achieve high printing resolution (for PL and SL), and (iii) rapid phase transformation for patterning sublayer of lamellar microstructures after printing on the platform (for PL). For MDIW 3D printing, the inks in the form of polymer solution and the liquid polymer were studied using (i) 20 wt.% polyvinyl alcohol (PVA)/water (PVA20-W) and E, (ii) 22 wt.% cellulose acetate butyrate

(CAB)/acetone (CAB22-A) and E, (iii) 30 wt.% halloysite/polyethylene glycol (PEG30-H) and E, and (iv) PEI and E-BN ink. The summary of all samples reported here, along with their abbreviations, is given in Table 1. The abbreviations are derived from ink material and ink processing conditions (*e.g.*, filler concentration, solvent, and temperatures). The PVA, CAB, PEG, and PEI were SL materials that displayed good solubility in common solvents, and the PL was E/E-BN. However, polymer solutions, such as PVA20-W/E and CAB22-A/E, revealed interfacial instability due to localized interlayer diffusion of solvents (*i.e.*, water and acetone) from higher (SL) to lower (PL) concentration region at the SL/PL interface (**Fig. S1**). To avoid the solvent molecules' diffusion at SL/PL interface, liquid polymers (*e.g.*, PEG and PEI) were studied as SL compositions. However, the higher wettability of PEG than PEI on the glass substrate caused the spreading of PEI during printing, which prevented the adhesion of the PL sublayer to the substrate (**Fig. S2**). Therefore, the PEI/E-BN material system was studied and proven with satisfied essential criteria, including material compatibility (during printing), phase separation capability (during printing), and structural stability (after printing).

Figure 2a represents the apparent viscosity of E-BN composite inks with different concentrations of 5-30 wt.% BNs (concentrations confirmed from thermogravimetric analyzer (TGA) (**Fig. S3**) as a function of shear stress. Generally, pure epoxy exhibits Newtonian flow, but adding fillers (*i.e.*, BNs, as shown in **Fig. S4**) can generate non-Newtonian properties.[58, 59] The composite inks showed an increase in zero shear viscosity from 11 (E) to 76 Pa.s (E-BN 25) which is attributed to physical cross-linking between the epoxy molecules and BNs. The magnitude of the shear-thinning behavior (*i.e.*, slope) near the 1/s shear rate increased with the higher BNs loading up to 30 wt.%. A slight shear thickening was observed for the ink 10-30 wt.% at a shear rate of less than 0.1 1/s, which may result from the transient yielding of the samples under shear.[60] When the shear rate increased from ≈ 0.1 to 1/s, the viscosity of the composite ink decreased, suggesting the aligned polymer chains and fillers along the shear direction and the decreased molecular entanglement.[61] However, the viscosity stabilized and reached around $\approx 20-30$ Pa/s for a shear rate of 1-100 1/s, within the theoretical shear rate range experienced during the layer formation process (**Fig. S5**).

The storage (G') and loss modulus (G") of the inks were investigated for E-BN and PEI inks at different testing ranges of shear rate (0.1–8000 1/s). For both the inks, the loss modulus was higher than the storage modulus, suggesting a dominant viscous behavior (Fig. S6). The dominance of loss modulus (tan delta (G"/G') > 1) was beneficial for the ink flowability and easy extrusion through the nozzle during the layer multiplication and printing process (Fig. 2b).[31, 62] The E-BN composite inks containing low BN concentration (< 20 wt.%) usually had low viscosity and high tan delta, causing the lateral spreading of 3D printed inks on the printing substrate. On the other hand, the composite ink containing high BN concentration (> 30 wt.%) caused clogging of the printing nozzle due to the formation of large aggregates (Fig. S7). Hence, the intermediate range of BN concentration, i.e., epoxy-25wt.% BN (E-BN25) as PL material provided optimal rheological properties and 3D printability via MDIW. Additionally, the inks should possess thixotropic properties to quickly recover the initial viscosity and thicken to retain the shape of the printed objects after the involvement of shear stress (Fig. S8).

Multi-material 3D printing has various challenges, *e.g.*, designing printable ink, interfacial instability, and layer-to-layer nonuniformity. The difference in the viscoelastic characteristics of the coextruding polymers and the presence of organic solvents is a critical contributing factor to the interfacial defects.[63] The weak secondary flow at the interface caused by viscoelastic effects (from the second normal stress differences) has been demonstrated to produce layer nonuniformities during extrusion.[64] Thus, these interfacial instabilities can be reduced or eliminated by matching the viscosity of the inks with the addition of fillers or applying heat to polymers. Thus, to obtain similar viscoelastic properties for PEI as SL and E-BN25 as PL, the PEI was heated from room temperature (RT) to 50° C for proper flow behavior. The apparent viscosity of the PEI gels measured at different temperatures showed that the gel's viscosity decreased due to increased polymer chain movements at higher temperatures (Fig. 2c). The PEI-50 (≈ 17 Pa/s) and E-BN25 (≈ 20 Pa/s) have a suitable viscosity match at the theoretical shear rate range (*i.e.*, 5–25 1/s). This viscosity matching limited the unfavorable interlayer diffusion at the PEI-50/E-BN25 interface from the time feedstocks combined at the spinneret till the multilayer structure was formed when exiting the MDIW 3D printing nozzle (**Fig. S9-S10**).[42]

The extruded E-BN25 composite ink had phase transformation depending on the photo-viscoelastic characteristics. The photopolymerization kinetics was evaluated with photo-rheology, monitoring the evolution of the storage modules (G') during UV-light irradiation. The liquid-to-solid transition of the ink after the photoirradiation was necessary for the storage modulus to exceed the loss modulus, *i.e.* when the thermomechanical energy was stored elastically than dissipating viscously.[65] Fig. 2d shows the high reactivity of acrylic-based epoxy over PEI, confirming their suitability for the MDIW 3D printing and wet etching process. The maximum reactivity of acrylic bonds was attained at ≈ 20 s, increasing storage modulus by 4-fold, with the gel point (*i.e.*, cross over of modulus (G' and G") obtained within 5 s of UV exposure. Once the E-BN ink exited the nozzle, the rapid phase transformation limited the interlayer diffusion in printed lamellar microstructures. On the other hand, the PEI-50 sublayer remaining unaffected by the UV-curing process was favorable for the subsequent removal during the wet etching process.

3.3 Multiphase Sublayer Formability

The superior printability of multi-material polymeric inks can facilitate 3D printed structures with high resolution, complex geometry, assembled nanostructure, and scalable micropatterning. To demonstrate the multi-material printability, the E-BN25 and PEI-50 inks were coextruded into different sublayers through the MDIW printhead, where a white sublayer was E-BN25 and a transparent sublayer was PEI (Fig. 3a). The morphology of multilayers was programmable via the multiplier number and size. The printed microstructures in Fig. 3a₁-a₃ show alternating sublayers of E-BN25 and PEI-50 with different layer numbers (e.g., < 32>, < 64>, and < 128>). The increase in < n > enabled thinner individual sublayers with curved morphology. The favorable rheological properties of the E-BN25 and PEI-50 inks rendered well-controlled fabrication of multilayer structures with high aspect ratios and fine micron resolutions. The multilayer structures can be scalably printed into a large area of \approx 400 cm² with an average thickness of \approx 350 µm within \approx 10 mins. The rapid phase transformation of the printed E-BN25 sublayer

by photopolymerization reaction constrained the PEI-50 sublayer between neighboring E-BN25 sublayers, with better regularity in higher < n >numbers (Fig. $3a_4$ - a_6).

The computational fluidic dynamic (CFD) simulations were used to understand the layer multiplication and printability process of multimaterial inks at a constant flow rate. Figure 3b shows CFD simulation for layer multiplication mechanism within each multiplier (#n) for the fabrication of < 32 > layers (i.e., green sublayer as E-BN25 and blue sublayer as PEI-50). The ink with similar viscoelastic properties passed through the #4 layer multiplier where < 16 > layers multiplied into < 32 > across the major axis, generating lamellar microstructure with sublayers of E-BN25 and PEI-50 in stacking. The zoom-in for layers formation mechanism within #3 and #4 is provided in the supporting figures (Fig. S11 and Table S2). Similarly, increasing layer multiplier numbers to #5 and #6 would generate the < 64 > and < 128 > layers as used during experimentation. Even though the volumetric flow rate of the inks was equal (1.5 ml/min), the E-BN25/PEI-50 sublayers experienced nonuniform shear stress spanning from the center to the periphery of the print head. This shearing inhomogeneity would cause a slight deviation in the width of individual sublayers (Fig. 3c).[63] The average width of PEI-50 and E-BN25 sublayers for < 128 > are 55 and 70 µm. respectively. The orientation of BNs within the sublayers was explored by XRD patterns with displayed (002), (100), and (004) peaks corresponding to the 27.1, 41.8, and 55.3° (Fig. 3d).[66] The intensity of the (002) diffraction peak was much stronger than (100). Generally, a higher intensity ratio between (002) and (100) diffraction peaks (I_{002}/I_{100}) means a higher orientation degree along the in-plane than planenormal direction. [67, 68] The increase in $I_{0.02}/I_{1.00}$ intensities ratios with higher layer number, <n>, indicated the improved orientation of BNs due to higher shear stress undergoing between adjacent sublayers.[69]

3.4 Etching Kinetics for Surface Micropatterning

A top-down wet etching process was combined with the bottom-up MDIW 3D printing to fabricate micropatterns (*i.e.*, microgrooves). A few suitable PEI solvents, including IPA (C_3H_7OH), ethanol (C_2H_5OH), and water (H_2O), were selected as etchants for the E-BN25/PEI-50 multilayer structures to understand the micropatterning kinetics (Fig. 4a-f). The hydrogen bonding between the PEI and these etchants was critical for the selective PEI elimination that was not observed for non-hydrogen-bonding solvents, such as acetone ((CH_3)₂CO).[70] The polymer etching and microgroove formation mechanism was attributed to the PEI dissolution at the polymer-etchant interface (Fig. 1c).[55]

During the etching process, the etchant dissolved the SL composition, and the material flowed from the substrate to the liquid upon agitation. The PEI dissolution percentage (SL material released in the etchant media in the unit of wt%) was measured via ($(w_i \cdot w_f)/w_i$)*100), where w_i was the initial weight of the sample before etching and w_f was the final weight of the sample after etching. The < 32 > layered samples were first used as an example to study the etching kinetics (Fig. 4a). The PEI dissolution increased as a function of time for all etchants, with the water dissolving PEI faster than ethanol and IPA. Similarly, water behaved as the most interactive solvent with PEI sublayers in < 64 > and < 128 > layered

structures (**Fig. S12**). The difference in PEI dissolution rates was correlated to (i) the etchant molecular size (*i.e.*, water = 0.28 nm, ethanol = 0.44 nm, and IPA = 0.6 nm), *i.e.*, the smaller the molecular size of the solvent, the faster the diffusion and polymer swelling,[71, 72] and (ii) wettability, *i.e.*, the better wettability of the etchants with PEI than E-BN25 would generate a stronger affinity of etchant for faster diffusion (**Fig. S13**).

As expected, the sublayer of E-BN25 exposed to UV curing showed no etching due to negligible dissolution because of the densely crosslinked structure, consistent with Fig. 2d. However, with the increase in soaking time, the E-BN25 layers were partially or entirely detached from the glass substrate for water and ethanol etchants (**Fig. S14**). This printing layer detachment could be due to more severe water or ethanol diffusion on substrate-layer interfaces, and thus, caused the mechanical failure (consistent with the larger interaction parameter in water and ethanol in Fig. 4d). Comparatively, the IPA solvent showed higher structural stability of E-BN25 micropatterns after etching (**Fig. S14**). Thus, the IPA was chosen as a preferential etchant for studying etching kinetics.

The etching rate of SL was expected to depend on a combination of four factors: etchant type, etching temperature, interaction time, and layer number. Therefore, we first investigated the effect of sublayer numbers on the etching rates. The higher < n> (i.e., < 64 > and < 128>) samples showed slower PEI dissolution than the lower < n> (i.e., < 32>), which was consistent at different etching periods and temperatures (Fig. 4b). The slower etching with the increase of < n > could be attributed to higher resistance to polymer removal due to more confined SL (i.e., by an average of 170, 125, and 55 µm for < 32>, < 64>, and < 128>, respectively, Fig. 3c). Moreover, the interfacial interaction area increases of the SL sublayer from 5.25 (for < 128>) to 12.75 mm² (for < 32>) also improved the PEI dissolution rates, as shown in Fig. 4b. Here, the interaction area is the top surface area of SL measured from multilayer film. The removal of the PEI SL as a function of etching time led to the formation of the microgroove patterns of different surface roughness values (Fig. S15). The material removal for higher sublayer numbers, <n>, was selective, stable, and precise, eventually leading to high-resolution micro features (Fig. 4b-c). Polymer dissolution is a thermodynamic phenomenon dependent on temperature. Thus, the etchant bath was heated from 25 to 35°C to study the temperature effects (Fig. 4c). The higher etchant bath temperature improved the polymer solubility. As a result, the etching rate consistently increased for samples of different layers (i.e., < 32>, < 64>, and < 128>) that were independent of the etching bath type (Fig. 4d and Fig. S16).

To theoretically understand the mechanism of the polymer etching that involved two transport processes, namely, diffusion and dissolution, the diffusion kinetics relationship $Q = kt^n$ was first generated.[73] Here, Q is the dissolution of SL in the etchant (%), k and n are constant, and t is time (min). Figure 4e shows the fitting of diffusion kinetics for PEI/IPA with < 32>, < 64>, and < 128 > layers, i.e., $Q_{<32>} = 0.03t^{0.62}$, $Q_{<64>} = 0.02t^{0.69}$, and $Q_{<128>} = 0.02t^{0.67}$, respectively. The exponent (n) value was fitted as 0.62, 0.69, and 0.67 for layers < 32>, < 64>, and < 128>, respectively, indicating the diffusion of PEI/etchant is a non-Fickian type diffusion (**Fig. S17-18**).[54] During the non-Fickian diffusion, solvent molecules penetrated through the

macro/microvoids formed at the polymer surface and bound to polymer molecules by hydrogen bonding, which led to the expansion and dissolution of the polymer chains.[73, 74] Additionally, the Flory-Huggins (FH) interaction parameters between polymer-etchant ($\chi_{polymer/etchant}$) were obtained as $\chi_{PEI/IPA} = 0.56$, $\chi_{PEI/ethanol} = 0.6$, and $\chi_{PEI/water} = 1.3$ (Fig. 4f derived using parameters in **Table S3**). This difference suggested the favorable miscibility of PEI in all solvents (*i.e.*, IPA, water, and ethanol) and higher swelling in water and IPA than ethanol, matching experimental observations (Fig. 4a).

The morphology of the etched micropattern was studied as a function of the interaction between the PEI sublayer and etchant. Figure 5a shows that as the etching time elapsed, the exposed channel width and depth increased, which led to the evolution from narrower/shallower to wider/deeper microgroove regions. For example, the microgroove width of the < 128 > layered samples increased from \approx 80 to 110 µm with an etching time of 1 to 20 min at RT (Fig. 5a). At the same time, the groove depth increased from \approx 20 to 35 µm under the same condition (Fig. 5a). The etching efficiency depended on the thermodynamic parameters (Fig. 4) and the confinement effects. Specifically, the PEI sublayer was quickly exposed to the etchant in the < 32>. In contrast, the finer E-BN sublayers with curved topology would confine PEI sublayers more robustly in the < 64 > and < 128 >, slowing down the dissolution during the etching process. To confirm the selective etching, the EDS in the multilayer samples showed wellcontrolled removal of the PEI sublayer (Fig. 5b) after etching via IPA at RT. In addition, the EDS line profile perpendicular to the sublayer texture direction showed a sharp and periodic drop in the boron chemical composition spanning the etched locations (Fig. 5c). Figure 5d also represents the cross-sectional morphology of the microgrooves fabricated via IPA (RT) etching for different < n > layers, demonstrating the SL etching effectiveness along the in-plane and out-of-plane directions as a function of etching time. The 3D surface topography of etched micropatterns also presented the consistent production of microgrooves with tunable dimensions and surface roughness (Fig. 5e).

3.5 Thermal Dissipation Demonstration

Micropatterned structures are helpful for directional heat transfer and creating thermal dissipation pathways, especially for high computing power electronics. Thus, our micropattern structures (e.g., channeled microfluidics) were used to demonstrate the heat dissipation efficiency with trapped air or cooling liquids for comparison purposes (Fig. 6a). Including BNs in composite microchannels could significantly increase the thermal properties by combining the effect of template design and the selective distribution of NPs. For example, the thermal properties of the E-BN composites were measured, showing a consistent increase in thermal conductivity (K_c) and thermal diffusivity (D_c) with higher BNs concentrations (Fig. 6b). The E-BN25 showed the highest thermal property improvement. The filler fraction within the composite microchannels has been no higher than 25 wt.% primarily due to 3D printing processability and to avoid nozzle clogging issues. Quantitatively, the thermal conductivity (K_c) values of E-BN25 micropatterned surfaces were calculated by the parallel models as 0.30, 0.18, and 0.24 W/mK for < 32>, < 64>, and < 128 > layers, respectively. However, the experimentally measured values were 0.19, 0.19, and 0.20 W/mK, mainly due to the instrument precision limit and trapped air during the hot

disk measurement (Fig. 6c). As a result, the difference in K_c was attributed to higher thermal resistance at the substrate/air interface in testing, which would increase the probability of phonon scattering.[75]

Due to the higher surface area (*i.e.*, 185, 164, and 141 mm² for < 32>, < 128>, and < 64> respectively), the < 32 > samples were demonstrated to contain coolants as two-phase heat transfer that occurs in micro or nano-sized passages, making these configurations increasingly essential to provide significant enhancement in heat management capabilities. Several cooling liquids, such as water, oil, and liquid metal (Ga-ln-Sn), are commonly used in microelectronics packaging because of their higher heat dissipation efficiency.[76] Theoretical simulations *via* the Finite Element Method (FEM) (see simulation details in SI section S3 and **Table S4**) predicted the average surface temperature and heat flux of E-BN25 < 32 > micropatterns (air-cooled vs. liquid-cooled). As a result, the fluids with higher heat transfer coefficients showed increased heat transfer from a heated micropatterning surface to fluids, thus lowering the average surface temperatures (*i.e.*, air > oil > water > liquid metal, Fig. 6d). Therefore, the water was used to demonstrate the cooling efficiency considering that coolants should be nonflammable, nontoxic, noncorrosive, and inexpensive in the microelectronics industry or computing facility management.

The electronics components have been designed to operate over a specified range, e.g., an upper limit of up to 80°C for industrial applications.[77] Therefore, E-BN25 < 32 > composites with and without water coolant were placed on the same hot stage at 80°C, with an infrared camera used to capture the IR images every 5°C (Fig. 6e). A calibrated thermocouple was used to record the real-time sample surface temperature. The surface temperature of the samples without coolant, E-BN25, increased much faster than one with the entrapped coolant, E-BN25C. A temperature difference as significant as $\approx 15^{\circ}$ C demonstrated the superior capability of the E-BN25C composite in heat dissipation (Fig. 6f). This difference was also confirmed by simulations, where the average surface temperature of E-BN25 composites with different layer numbers was lowered to 61.32°C (< 32>), 60.75°C (< 64>), and 60.27°C (< 128>) from 75.92°C (< 32>), 76.04°C (< 64>), and 75.71°C (< 128>) (Table S5), demonstrating highperformance micro cooling systems that can enable faster heat dissipation benefiting conventional heat sink microstructures. The BN nanoparticles within micropatterns are preferentially aligned along the printing direction and interconnected, forming thermal conductive pathways to adjacent coolant regions. The nanoscale heat transfer within a substrate and micro heat exchange between two phases (i.e., substrate and coolant) improved the heat dissipation in the plane direction, and lowered surface temperature in the through-plane direction was observed. The FEM simulation contour mapping also indicated heat accumulation and higher surface temperature for E-BN25 planar than micropattern structures (Fig. 6g). By contrast, the trapped cooling agents in E-BN25C can significantly enhance the heat transfer along the out-of-plane direction without much heat accumulation (Fig. 6g). Besides, E-BN25 micropattern structure exhibit superior electrically insulating property. Thus, a thermally conductive but electrically insulating film is supposed to be an efficient thermal management structure to conduct the heat from electronic components to the environment, improving the components' efficiency and lifespan.

4. Conclusion

In summary, we have demonstrated a technique combining unique 3D printing (i.e., MDIW) and wet etching to create micropatterns (i.e., an array of micro-grooves). The in-house developed MDIW was used to fabricate the lamellar structure with alternating sublayers of UV-curable PL and wet-etchable SL. The morphology (i.e., layer number and width) of multilayer 3D printed structures were fabricated by controlling the polymer composition, particle loading, ink viscoelasticity, phase transformation, shear stress, and extrusion rates. The rapid phase transformation of PL retained the printed microstructures and enabled "micro-confinement" of SL for subsequent wet etching. As a result, the printed multilayer structures had well-controlled sublayer dimensions, ranging from ≈ 50 to 200 µm depending on the layer multiplying procedures. The selective dissolution of SL formed the micropatterns due to polymer-solvent interdiffusion during the wet-etching process. The etching kinetics (e.g., time, temperature, interaction parameters), pattern microstructures, and etchant types significantly influenced the micropatterning geometries and morphologies. Besides, the micropatterned surfaces with confined BNs-enabled thermally conductive behaviors and micropattern-contained liquid coolant further increased heat dissipation efficiency. The polymer-polymer and polymer-solvent interaction phenomena helped multilayer printability and micropatterning via controlled polymer dissolution to establish the processing-structure-property relationship. Our micropatterning technique opens a new pathway that enables the fabrication of hierarchical structures through a printing-solvent-free, maskless, scalable, and cost-effective process compared to conventional patterning protocols. MDIW 3D printing also shows high compatibility with various polymeric and metallic inks, suggesting possibilities to design mechanical, thermal, electrical, optical, and magnetic properties for broad applications.

Declarations

ASSOCIATED CONTENT

Supporting Information:

Additional information included details related to 1. Ink rheology and 3D printing processability like microstructure of trial printing materials, wettability of printing inks, BNs morphology, TGA of composite inks, viscoelastic properties of ink, theoretical shear rate calculations during MDIW 3D printing, MDIW 3D printing defects, interfacial behavior of printing inks, fluid flow simulation of printing inks within printhead; 2. Etching dynamics like PEI dissolution behavior for <64> and <128> sublayers, contact angle measurement of printing material and etchants, micropatterns surface roughness, PEI diffusion kinetics, table of solubility parameter of etchant for Flory Huggins calculations; Thermal dissipation demonstrations like Ansys simulation for temperature distribution of etched micropattern surfaces and table of calculated thermal properties like temperature and heat flux for etched micropatterns.

Author contributions:

S. Jambhulkar and K. Song conceptualized and designed a research objective; S. Jambhulkar performed experiments, analyzed results, performed theoretical calculations, and drafted manuscript; D. Ravichandran designed MDIW 3D printing setup and performed fluidic simulation; V. Thippanna, and D. Patil assisted with experiments of 3D printing. All authors reviewed the final manuscript.

The authors declare no competing financial interest.

AUTHOR INFORMATION

Corresponding Author

E-mail: kenan.song@asu.edu

FUNDING

We acknowledge the financial support from the NSF EAGER (Award Abstract #1902172), NSF CAREER (Award #2145895), ONR NEPTUNE (N00014-22-1-2105), AFOSR (FA9550-22-1-0263), BSF (2020102), and ACS PRF (#62371-ND10).

ACKNOWLEDGMENT

We would like to thank Dr. D. Bhate from 3DX research for the use of the Keyence 3D Optical profilometer at ASU. We thank Dr. B. Kwon for providing help to use the hot disk at ASU.

References

- 1. Wooh S, Yoon H, Jung J-H, et al (2013) Efficient Light Harvesting with Micropatterned 3D Pyramidal Photoanodes in Dye-Sensitized Solar Cells. Adv Mater 25:3111–3116. https://doi.org/10.1002/adma.201300085
- 2. Feng W, Chai Y, Forth J, et al (2019) Harnessing liquid-in-liquid printing and micropatterned substrates to fabricate 3-dimensional all-liquid fluidic devices. Nat Commun 10:1095. https://doi.org/10.1038/s41467-019-09042-y
- 3. Han B, Huang Y, Li R, et al (2014) Bio-inspired networks for optoelectronic applications. Nat Commun 5:5674. https://doi.org/10.1038/ncomms6674
- 4. Kim M, Brown DK, Brand O (2020) Nanofabrication for all-soft and high-density electronic devices based on liquid metal. Nat Commun 11:1002. https://doi.org/10.1038/s41467-020-14814-y
- 5. Quist AP, Oscarsson S (2010) Micropatterned surfaces: techniques and applications in cell biology. Expert Opinion on Drug Discovery 5:569–581. https://doi.org/10.1517/17460441.2010.489606
- 6. Jambhulkar S, Liu S, Vala P, et al (2021) Aligned Ti ₃ C ₂ T _x MXene for 3D Micropatterning *via*Additive Manufacturing. ACS Nano 15:12057–12068. https://doi.org/10.1021/acsnano.1c03388
- 7. Barad H-N, Kwon H, Alarcón-Correa M, Fischer P (2021) Large Area Patterning of Nanoparticles and Nanostructures: Current Status and Future Prospects. ACS Nano 15:5861–5875.

- https://doi.org/10.1021/acsnano.0c09999
- 8. Kim Y, Kim T, Lee J, et al (2021) Tailored Graphene Micropatterns by Wafer-Scale Direct Transfer for Flexible Chemical Sensor Platform. Adv Mater 33:2004827. https://doi.org/10.1002/adma.202004827
- 9. Topolniak I, Elert AM, Knigge X, et al (2022) High-Precision Micropatterning of Polydopamine by Multiphoton Lithography. Advanced Materials 34:2109509. https://doi.org/10.1002/adma.202109509
- 10. Pfeiffer F, Felix NM, Neuber C, et al (2007) Physical Vapor Deposition of Molecular Glass Photoresists: A New Route to Chemically Amplified Patterning. Adv Funct Mater 17:2336–2342. https://doi.org/10.1002/adfm.200600717
- 11. Obst M, Arnauts G, Cruz AJ, et al (2021) Chemical Vapor Deposition of Ionic Liquids for the Fabrication of Ionogel Films and Patterns. Angewandte Chemie Intl Edit 60:25668–25673. https://doi.org/10.1002/anie.202110022
- 12. Li P, Dou X, Schönherr H (2019) Micropatterning and nanopatterning with polymeric materials for advanced biointerface-controlled systems. Polym Int 68:1015–1032. https://doi.org/10.1002/pi.5770
- 13. Grzelczak M, Vermant J, Furst EM, Liz-Marzán LM (2010) Directed Self-Assembly of Nanoparticles. ACS Nano 4:3591–3605. https://doi.org/10.1021/nn100869j
- 14. Yang GG, Choi HJ, Han KH, et al (2022) Block Copolymer Nanopatterning for Nonsemiconductor Device Applications. ACS Appl Mater Interfaces 14:12011–12037. https://doi.org/10.1021/acsami.1c22836
- 15. Kiruthika S, Radha B (2020) Direct Micromolding of Bimetals and Transparent Conducting Oxide Using Metal-TOABr Complexes as Single-Source Precursors. ACS Omega 5:20739-20745. https://doi.org/10.1021/acsomega.0c00407
- 16. Jung W, Jang S, Cho S, et al (2020) Recent Progress in Simple and Cost-Effective Top-Down Lithography for ≈10 nm Scale Nanopatterns: From Edge Lithography to Secondary Sputtering Lithography. Adv Mater 32:1907101. https://doi.org/10.1002/adma.201907101
- 17. Rogers JA, Lee HH (2008) Unconventional Nanopatterning Techniques and Applications. John Wiley & Sons, Inc., Hoboken, NJ, USA
- 18. Hosaka K, Tagami J, Nishitani Y, et al (2007) Effect of wet vs. dry testing on the mechanical properties of hydrophilic self-etching primer polymers. Eur J Oral Sci 115:239–245. https://doi.org/10.1111/j.1600-0722.2007.00452.x
- 19. Puliyalil H, Cvelbar U (2016) Selective Plasma Etching of Polymeric Substrates for Advanced Applications. Nanomaterials 6:108. https://doi.org/10.3390/nano6060108
- 20. Kwak D, Lim JA, Kang B, et al (2013) Self-Organization of Inkjet-Printed Organic Semiconductor Films Prepared in Inkjet-Etched Microwells. Adv Funct Mater 23:5224–5231. https://doi.org/10.1002/adfm.201300936

- 21. de Gans B-J, Hoeppener S, Schubert US (2006) Polymer-Relief Microstructures by Inkjet Etching. Adv Mater 18:910–914. https://doi.org/10.1002/adma.200502051
- 22. Bao B, Jiang J, Li F, et al (2015) Fabrication of Patterned Concave Microstructures by Inkjet Imprinting. Adv Funct Mater 25:3286–3294. https://doi.org/10.1002/adfm.201500908
- 23. de Beer MP, van der Laan HL, Cole MA, et al (2019) Rapid, continuous additive manufacturing by volumetric polymerization inhibition patterning. Sci Adv 5:eaau8723. https://doi.org/10.1126/sciadv.aau8723
- 24. Jambhulkar S, Xu W, Ravichandran D, et al (2020) Scalable Alignment and Selective Deposition of Nanoparticles for Multifunctional Sensor Applications. Nano Lett 20:3199–3206. https://doi.org/10.1021/acs.nanolett.9b05245
- 25. Jambhulkar S, Xu W, Franklin R, et al (2020) Integrating 3D printing and self-assembly for layered polymer/nanoparticle microstructures as high-performance sensors. J Mater Chem C 8:9495–9501. https://doi.org/10.1039/D0TC02660C
- 26. Ahn D, Stevens LM, Zhou K, Page ZA (2020) Rapid High-Resolution Visible Light 3D Printing. ACS Cent Sci 6:1555–1563. https://doi.org/10.1021/acscentsci.0c00929
- 27. Kelly BE, Bhattacharya I, Heidari H, et al (2019) Volumetric additive manufacturing via tomographic reconstruction. Science 363:1075–1079. https://doi.org/10.1126/science.aau7114
- 28. Tumbleston JR, Shirvanyants D, Ermoshkin N, et al (2015) Continuous liquid interface production of 3D objects. Science 347:1349–1352. https://doi.org/10.1126/science.aaa2397
- 29. Loke G, Yuan R, Rein M, et al (2019) Structured multimaterial filaments for 3D printing of optoelectronics. Nat Commun 10:4010. https://doi.org/10.1038/s41467-019-11986-0
- 30. Coelho S, Baek J, Walsh J, et al (2022) Direct-laser writing for subnanometer focusing and single-molecule imaging. Nat Commun 13:647. https://doi.org/10.1038/s41467-022-28219-6
- 31. Lewis JA (2006) Direct Ink Writing of 3D Functional Materials. Adv Funct Mater 16:2193–2204. https://doi.org/10.1002/adfm.200600434
- 32. Reiser A, Lindén M, Rohner P, et al (2019) Multi-metal electrohydrodynamic redox 3D printing at the submicron scale. Nat Commun 10:1853. https://doi.org/10.1038/s41467-019-09827-1
- 33. Park J-U, Hardy M, Kang SJ, et al (2007) High-resolution electrohydrodynamic jet printing. Nature Mater 6:782–789. https://doi.org/10.1038/nmat1974
- 34. Jung W, Jung Y-H, Pikhitsa PV, et al (2021) Three-dimensional nanoprinting via charged aerosol jets. Nature 592:54–59. https://doi.org/10.1038/s41586-021-03353-1
- 35. Su W, Cook BS, Fang Y, Tentzeris MM (2016) Fully inkjet-printed microfluidics: a solution to low-cost rapid three-dimensional microfluidics fabrication with numerous electrical and sensing applications. Sci Rep 6:35111. https://doi.org/10.1038/srep35111
- 36. Xu W, Jambhulkar S, Zhu Y, et al (2021) 3D printing for polymer/particle-based processing: A review. Composites Part B: Engineering 223:109102. https://doi.org/10.1016/j.compositesb.2021.109102

- 37. Xu W, Jambhulkar S, Ravichandran D, et al (2021) 3D Printing-Enabled Nanoparticle Alignment: A Review of Mechanisms and Applications. Small 17:2100817. https://doi.org/10.1002/smll.202100817
- 38. Elder B, Neupane R, Tokita E, et al (2020) Nanomaterial Patterning in 3D Printing. Adv Mater 32:1907142. https://doi.org/10.1002/adma.201907142
- 39. Ravichandran D, Xu W, Kakarla M, et al (2021) Multiphase direct ink writing (MDIW) for multilayered polymer/nanoparticle composites. Additive Manufacturing 47:102322. https://doi.org/10.1016/j.addma.2021.102322
- 40. Xu W, Ravichandran D, Jambhulkar S, et al (2021) Hierarchically Structured Composite Fibers for Real Nanoscale Manipulation of Carbon Nanotubes. Adv Funct Mater 31:2009311. https://doi.org/10.1002/adfm.202009311
- 41. Xu W, Franklin R, Ravichandran D, et al (2022) Continuous Nanoparticle Patterning Strategy in Layer-Structured Nanocomposite Fibers. Adv Funct Materials 2204731. https://doi.org/10.1002/adfm.202204731
- 42. Ravichandran D, Xu W, Kakarla M, et al (2021) Multiphase direct ink writing (MDIW) for multilayered polymer/nanoparticle composites. Additive Manufacturing 47:102322. https://doi.org/10.1016/j.addma.2021.102322
- 43. Rasul MG, Cheng M, Jiang Y, et al (2022) Direct Ink Printing of PVdF Composite Polymer Electrolytes with Aligned BN Nanosheets for Lithium-Metal Batteries. ACS Nanosci Au 2:297–306. https://doi.org/10.1021/acsnanoscienceau.1c00056
- 44. Tao Y, Kong F, Li Z, et al (2021) A review on voids of 3D printed parts by fused filament fabrication. Journal of Materials Research and Technology 15:4860–4879. https://doi.org/10.1016/j.jmrt.2021.10.108
- 45. Guo H, Zhao H, Niu H, et al (2021) Highly Thermally Conductive 3D Printed Graphene Filled Polymer Composites for Scalable Thermal Management Applications. ACS Nano 15:6917–6928. https://doi.org/10.1021/acsnano.0c10768
- 46. Ravichandran D, Ahmed RJ, Banerjee R, et al (2022) Multi-material 3D printing-enabled multilayers for smart actuation *via* magnetic and thermal stimuli. J Mater Chem C 10.1039.D2TC01109C. https://doi.org/10.1039/D2TC01109C
- 47. Grundke K, Michel S, Osterhold M (2000) Surface tension studies of additives in acrylic resin-based powder coatings using the Wilhelmy balance technique. Progress in Organic Coatings 39:101–106. https://doi.org/10.1016/S0300-9440(00)00129-6
- 48. Bellettini IC, Eising R, Felippe AC, et al (2015) ASSOCIATION OF BRANCHED POLYETHYLENE IMINE WITH SURFACTANTS IN AQUEOUS SOLUTION. Química Nova. https://doi.org/10.5935/0100-4042.20150085
- 49. Penfold J, Tucker I, Thomas RK, et al (2007) The Impact of Electrolyte on the Adsorption of Sodium Dodecyl Sulfate/Polyethyleneimine Complexes at the Air–Solution Interface. Langmuir 23:3690–3698. https://doi.org/10.1021/la063017p

- 50. Lee MY, Lee JH, Chung JW, Kwak S-Y (2018) Hydrophilic and positively charged polyethylenimine-functionalized mesoporous magnetic clusters for highly efficient removal of Pb(II) and Cr(VI) from wastewater. Journal of Environmental Management 206:740–748. https://doi.org/10.1016/j.jenvman.2017.10.051
- 51. Uzal N, Ates N, Saki S, et al (2017) Enhanced hydrophilicity and mechanical robustness of polysulfone nanofiber membranes by addition of polyethyleneimine and Al2O3 nanoparticles. Separation and Purification Technology 187:118–126. https://doi.org/10.1016/j.seppur.2017.06.047
- 52. Wang T, Zhang G, Zhang B, et al (2021) Oriented Boron Nitride Nanosheet Films for Thermal Management and Electrical Insulation in Electrical and Electronic Equipment. ACS Appl Nano Mater 4:4153–4161. https://doi.org/10.1021/acsanm.1c00484
- 53. Han J, Du G, Gao W, Bai H (2019) An Anisotropically High Thermal Conductive Boron Nitride/Epoxy Composite Based on Nacre-Mimetic 3D Network. Adv Funct Mater 29:1900412. https://doi.org/10.1002/adfm.201900412
- 54. Encapsulation Technologies for Electronic Applications. Elsevier
- 55. Miller-Chou BA, Koenig JL (2003) A review of polymer dissolution. Progress in Polymer Science 28:1223-1270. https://doi.org/10.1016/S0079-6700(03)00045-5
- 56. Schaffner M, Rühs PA, Coulter F, et al (2017) 3D printing of bacteria into functional complex materials. Sci Adv 3:eaao6804. https://doi.org/10.1126/sciadv.aao6804
- 57. Zhao S, Siqueira G, Drdova S, et al (2020) Additive manufacturing of silica aerogels. Nature 584:387–392. https://doi.org/10.1038/s41586-020-2594-0
- 58. Cheng M, Ramasubramanian A, Rasul MG, et al (2021) Direct Ink Writing of Polymer Composite Electrolytes with Enhanced Thermal Conductivities. Adv Funct Mater 31:2006683. https://doi.org/10.1002/adfm.202006683
- 59. Shen K, Ding J, Yang S (2018) 3D Printing Quasi-Solid-State Asymmetric Micro-Supercapacitors with Ultrahigh Areal Energy Density. Adv Energy Mater 8:1800408. https://doi.org/10.1002/aenm.201800408
- 60. Yirmibesoglu OD, Simonsen LE, Manson R, et al (2021) Multi-material direct ink writing of photocurable elastomeric foams. Commun Mater 2:82. https://doi.org/10.1038/s43246-021-00186-3
- 61. Yuk H, Lu B, Lin S, et al (2020) 3D printing of conducting polymers. Nat Commun 11:1604. https://doi.org/10.1038/s41467-020-15316-7
- 62. Saadi MASR, Maguire A, Pottackal NT, et al (2022) Direct Ink Writing: A 3D Printing Technology for Diverse Materials. Advanced Materials 34:2108855. https://doi.org/10.1002/adma.202108855
- 63. Agassant J-F, Demay Y (2022) Investigation of the Polymer Coextrusion Process: A Review. Polymers 14:1309. https://doi.org/10.3390/polym14071309
- 64. Lu B, Zhang H, Maazouz A, Lamnawar K (2021) Interfacial Phenomena in Multi-Micro-/Nanolayered Polymer Coextrusion: A Review of Fundamental and Engineering Aspects. Polymers 13:417. https://doi.org/10.3390/polym13030417

- 65. Cortés A, Cosola A, Sangermano M, et al (2021) DLP 4D-Printing of Remotely, Modularly, and Selectively Controllable Shape Memory Polymer Nanocomposites Embedding Carbon Nanotubes. Adv Funct Mater 31:2106774. https://doi.org/10.1002/adfm.202106774
- 66. Guerra V, Wan C, Degirmenci V, et al (2018) 2D boron nitride nanosheets (BNNS) prepared by high-pressure homogenisation: structure and morphology. Nanoscale 10:19469–19477. https://doi.org/10.1039/C8NR06429F
- 67. Lin Z, Liu Y, Raghavan S, et al (2013) Magnetic Alignment of Hexagonal Boron Nitride Platelets in Polymer Matrix: Toward High Performance Anisotropic Polymer Composites for Electronic Encapsulation. ACS Appl Mater Interfaces 5:7633–7640. https://doi.org/10.1021/am401939z
- 68. Han G, Zhang D, Kong C, et al (2022) Flexible, thermostable and flame-resistant epoxy-based thermally conductive layered films with aligned ionic liquid-wrapped boron nitride nanosheets via cyclic layer-by-layer blade-casting. Chemical Engineering Journal 437:135482. https://doi.org/10.1016/j.cej.2022.135482
- 69. Zhong B, Zou J, An L, et al (2019) The effects of the hexagonal boron nitride nanoflake properties on the thermal conductivity of hexagonal boron nitride nanoflake/silicone rubber composites. Composites Part A: Applied Science and Manufacturing 127:105629. https://doi.org/10.1016/j.compositesa.2019.105629
- 70. Du M-X, Yuan Y-F, Zhang J-M, Liu C-Y (2022) Hydrogen-Bonding Interactions in Polymer-Organic Solvent Mixtures. Macromolecules 55:4578-4588. https://doi.org/10.1021/acs.macromol.2c00799
- 71. Chan TC, Li HT, Li KY (2015) Effects of Shapes of Solute Molecules on Diffusion: A Study of Dependences on Solute Size, Solvent, and Temperature. J Phys Chem B 119:15718–15728. https://doi.org/10.1021/acs.jpcb.5b10550
- 72. P. Gall T, Lasky RC, Kramer EJ (1990) Case II diffusion: effect of solvent molecule size. Polymer 31:1491–1499. https://doi.org/10.1016/0032-3861(90)90156-S
- 73. Jasso-Gastinel CF (2017) Gradients in Homopolymers, Blends, and Copolymers. In: Modification of Polymer Properties. Elsevier, pp 185–210
- 74. Baij L, Hermans JJ, Keune K, Iedema PD (2018) Time-Dependent ATR-FTIR Spectroscopic Studies on Solvent Diffusion and Film Swelling in Oil Paint Model Systems. Macromolecules 51:7134–7144. https://doi.org/10.1021/acs.macromol.8b00890
- 75. Harter JR, Palmer TS, Greaney PA (2020) Predicting mesoscale spectral thermal conductivity using advanced deterministic phonon transport techniques. In: Advances in Heat Transfer. Elsevier, pp 335–488
- 76. Sohel Murshed SM, Nieto de Castro CA (2017) A critical review of traditional and emerging techniques and fluids for electronics cooling. Renewable and Sustainable Energy Reviews 78:821–833. https://doi.org/10.1016/j.rser.2017.04.112
- 77. Pastukhov VG, Maidanik YuF, Vershinin CV, Korukov MA (2003) Miniature loop heat pipes for electronics cooling. Applied Thermal Engineering 23:1125–1135. https://doi.org/10.1016/S1359-4311(03)00046-2

Figures

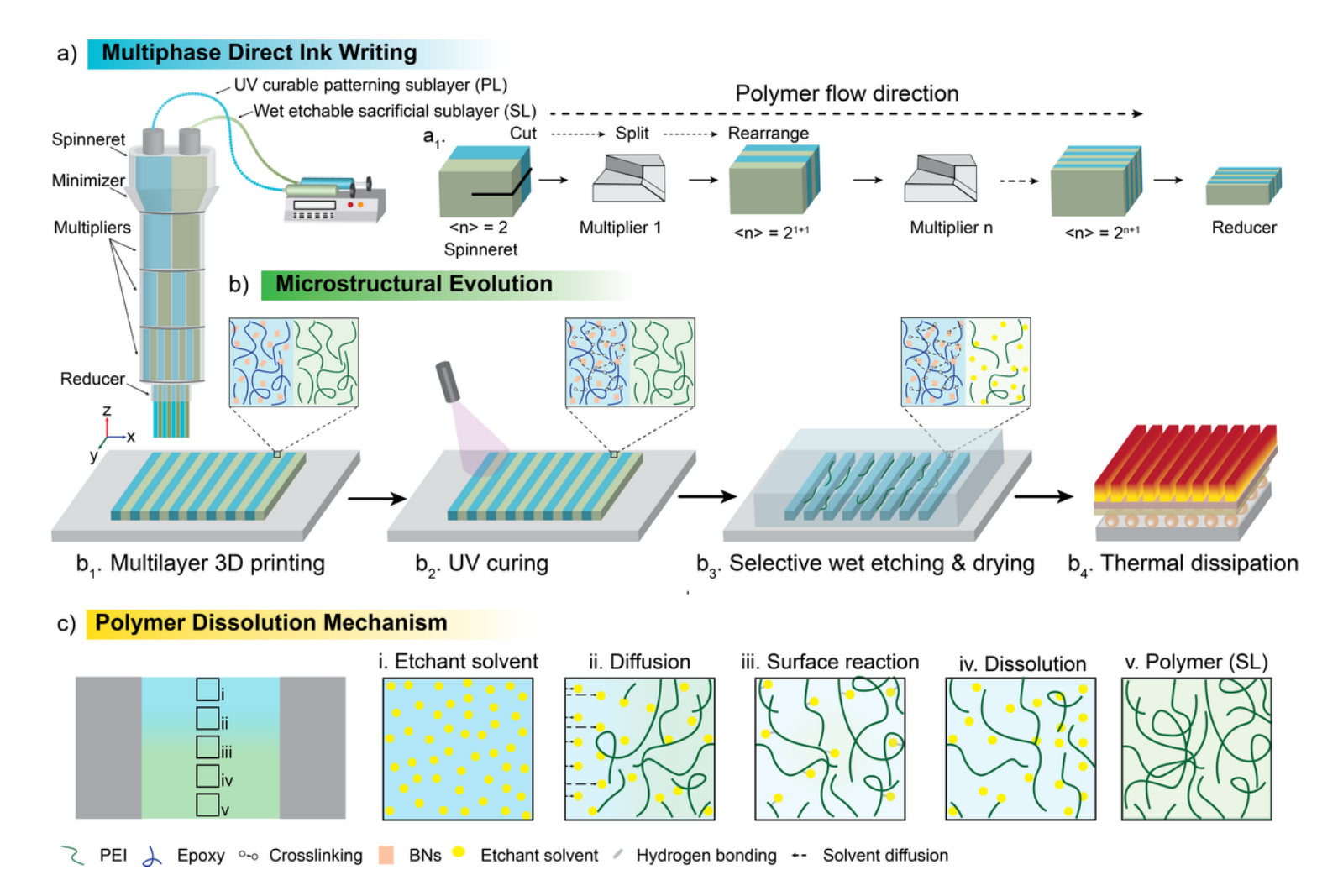


Figure 1

Fabrication strategy for micropatterns with MDIW 3D printing and wet etching. a) Multilayer 3D printing with MDIW demonstrating a_1) the sublayer formation mechanism enabled by printhead components consisting of a spinneret, a minimizer, multipliers, and a reducer, b) the distinct microstructural change in the patterning layer (PL) and sacrificial layer (SL) at different manufacturing stages, such as b_1) 3D printing, b_2) UV curing, b_3) wet etching followed by drying to form permanent patterns, b_4) demonstrating micropatterned surfaces for heat dissipation applications in semiconductor packaging, and c) selective wet etching of SL upon exposure to etchant and its microstructural evolution as a function of time, showing intermediate etching stages between the etchant solvent and SL polymer.

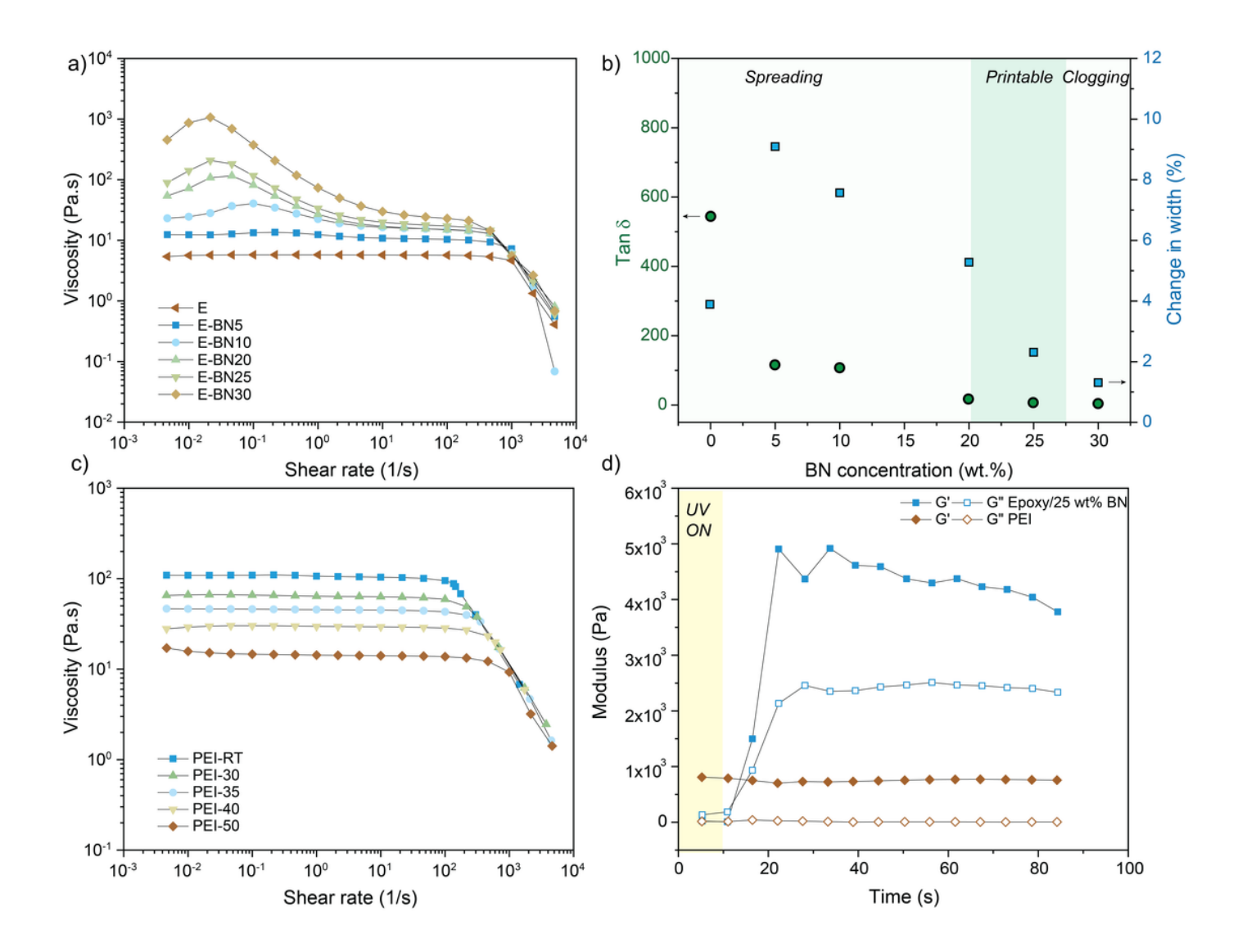


Figure 2

Rheological properties of feedstock inks used for MDIW 3D printing. a) The apparent viscosity of the epoxy ink with and without BNs fillers (Table 1) as a function of the shear rates, b) tan delta (d) and dimensional change (*i.e.*, the printing line width) of E-BN composite inks containing varying BNs concentrations, c) the apparent viscosity of PEI measured at different temperatures, d) photo-rheology measurements of the evolution of storage modulus (G') and loss modulus (G") during UV light irradiation (light wavelength \approx 365 nm and switched off after 10 sec) for both patterning layer (*i.e.*, E-BN25) and sacrificial layer (*i.e.*, PEI-50) samples.

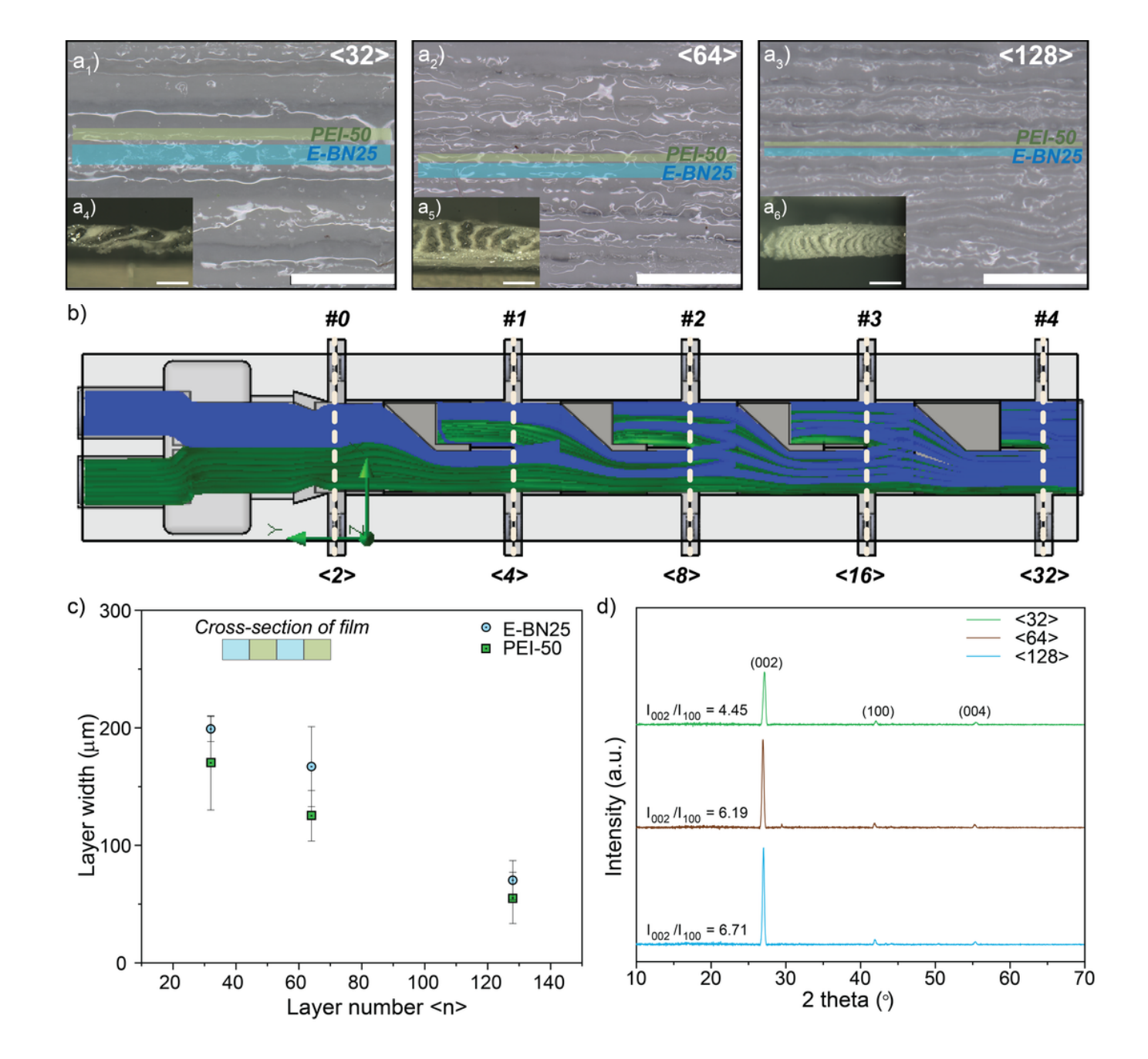


Figure 3

Microstructure of the 3D printed multilayer structures. a_1 - a_3) E-BN25 and PEI-50 with different layer numbers <32>, <64>, and <128> (scale bar 1200 µm). a_4 - a_6) Inset optical images show the cross-sectional morphology of the printed microlayers (scale bar 500 µm), b) computational fluidic dynamic (CFD) simulations of E-BN25 and PEI-50 inks for <32> as an example to show the layer multiplying mechanism (*i.e.*, green sublayer as E-BN25 and blue sublayer as PEI-50, see more details in Fig. S11 and modeling information in SI), c) dimensions of the E-BN25 and PEI sublayers exhibit consistent layer size evolutions (*i.e.*, width values decrease vs. higher layer numbers), and d) XRD patterns of the E-BN25 multilayer composites with improved BNs orientations as layers multiply.

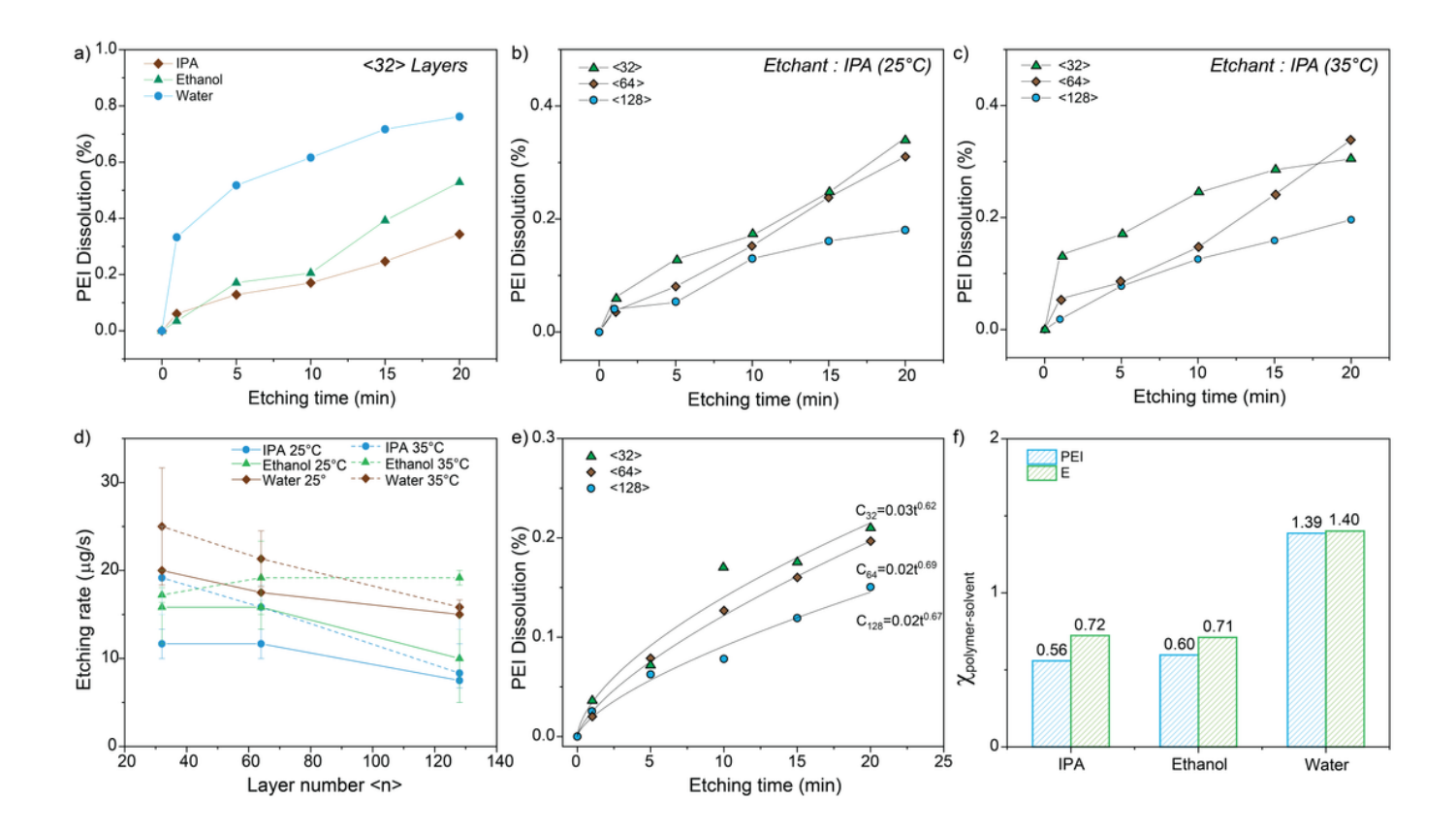


Figure 4

Etching kinetics of E-BN25/PEI-50 multilayer structures. a) PEI sublayer dissolution (%) for <32> by different etchants (*i.e.*, IPA, ethanol, and water) as a function of etching time (min), PEI dissolution by IPA etchant at b) room temperature (RT \approx 25°C) and c) 35°C as a function of <n> (*i.e.*, n=32, 64 and, 128), d) etching rate (mg/s) of PEI sublayer as a function of <n> for different etchants (*i.e.*, IPA, ethanol, and water) and bath temperatures (at RT (\approx 25°C) and 35°C, respectively), e) PEI sublayer diffusion kinetics for the <32>, <64>, and <128> layers in IPA(RT) etchant, and f) Flory-Huggins interaction parameters ($c_{polymer/etchant}$) for PEI and E for IPA, ethanol, and water etchants.

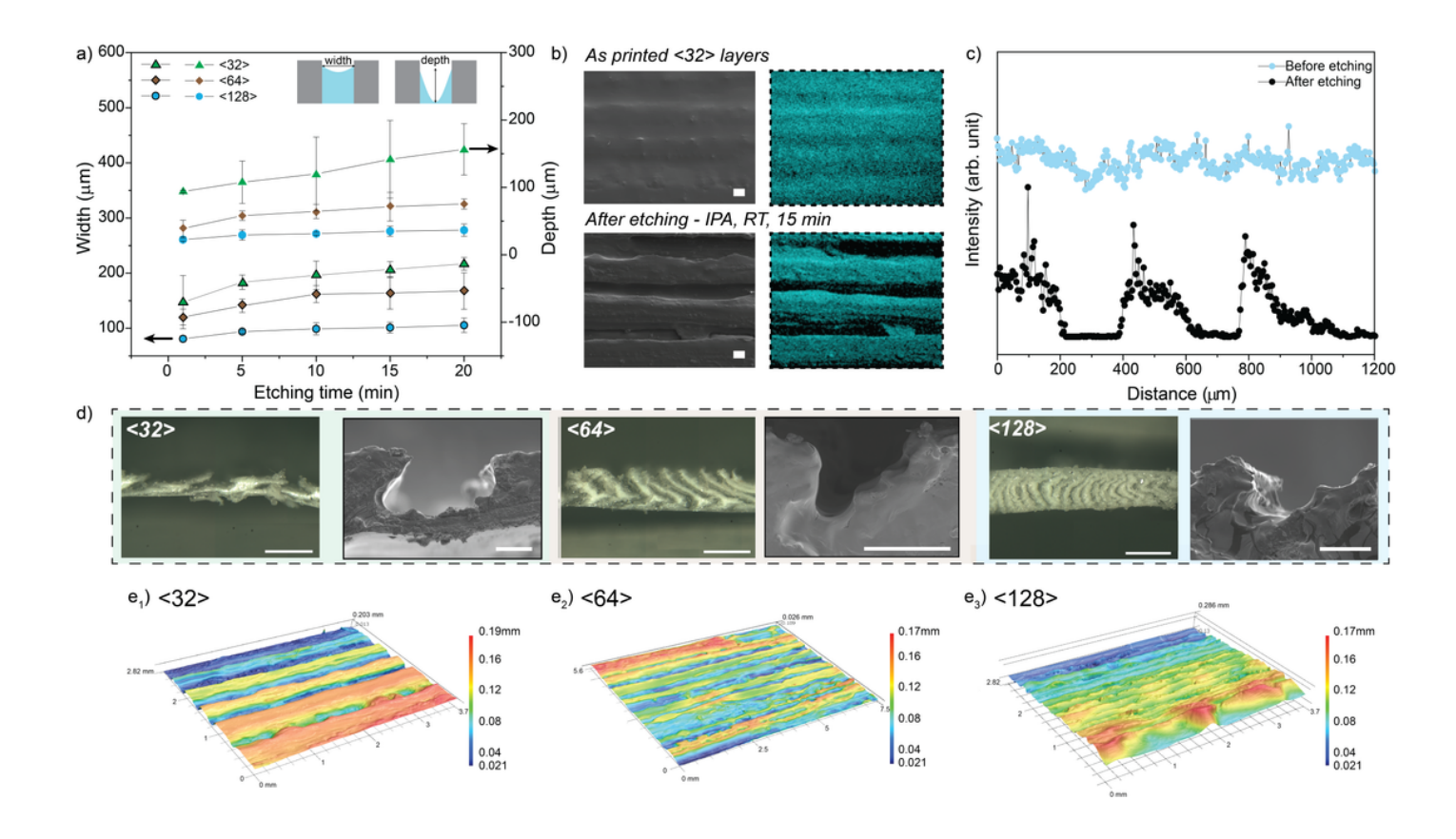


Figure 5

Microstructure evolution of MDIW micropatterns. a) Width and depth plot of micropatterns depending on the etching time for different layer numbers, b) surface elemental distribution spectroscopy (EDS) mapping of the <32> before and after etching (boron tracing), c) EDS line profile of boron across the patterned surfaces before and after etching, d) optical and SEM images show the cross-sectional view of micropatterns (*i.e.*, microgrooves) fabricated *via* different multiplying/layering after IPA etching at RT (scale bar 500 μ m and 100 μ m for optical and SEM, respectively), and the corresponding 3D surface topography of etched samples showing the formation of microgrooves after IPA etching at RT for e₁) <32>, e₂) <64>, and e₃) <128> layers.

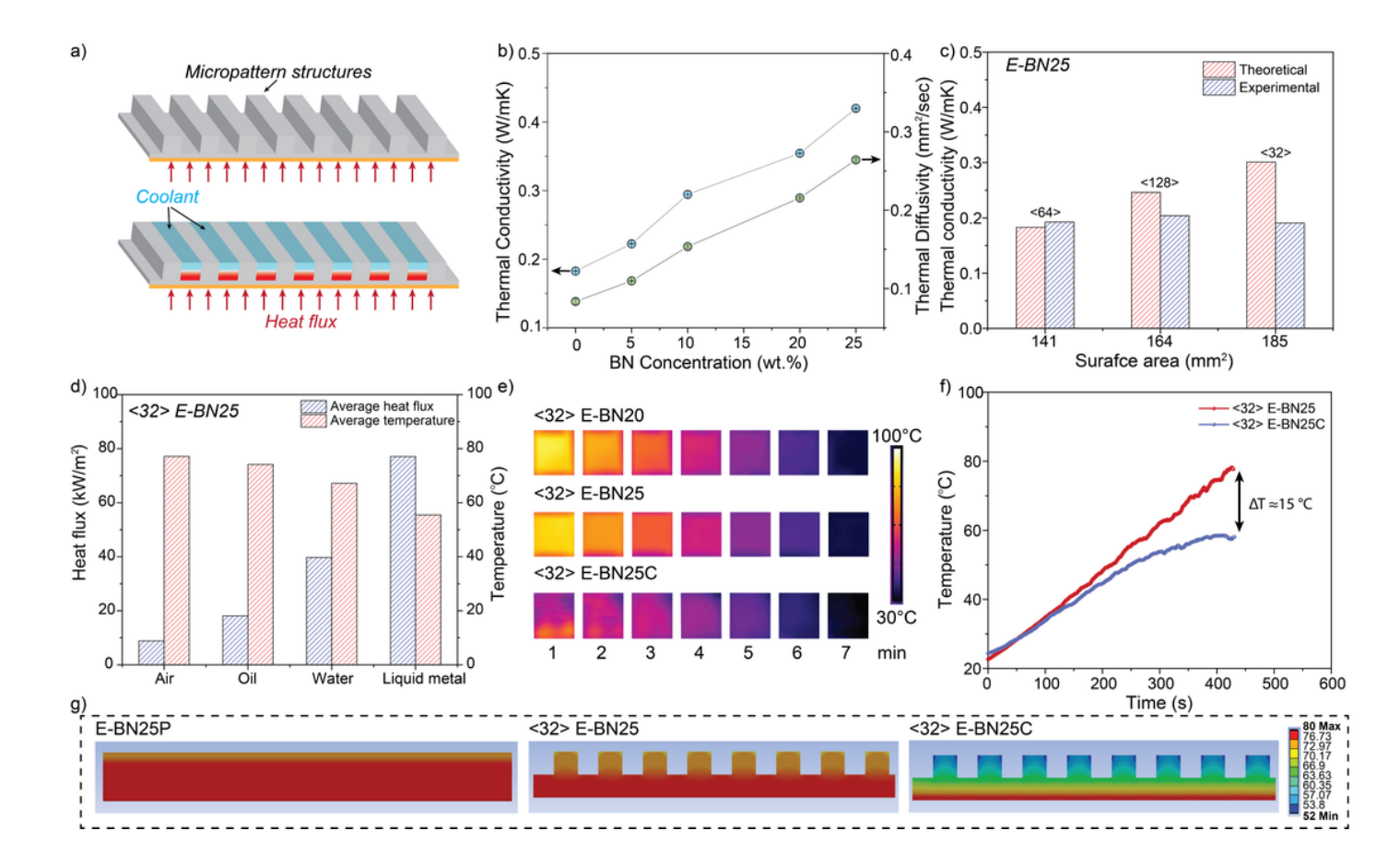


Figure 6

Thermal capability demonstrations. a) The schematic illustration of microgrooves as channeled microfluidic cooling systems, b) measured thermal property (*i.e.*, conductivity, diffusivity) values of the composite as a function of BN concentrations, c) theoretical and experimental thermal conductivity values of E-BN25 for as a function of measured surface area (*i.e.*, <32> layer number exposed the highest surface area due to the shape distortion, as shown in Fig. 5d), d) average surface temperature and average heat flux of E-BN25 <32> with air (no coolant) and coolant liquids (*i.e.*, oil, water, and liquid metal) confined between microchannels (as shown in schematic 6a) for <32> samples, e) IR images of composite microchannel surfaces for E-BN20, E-BN25, and E-BN25C (Table 1), f) comparison of the surface temperature of E-BN25 and E-BN25C for <32>, and g) simulation results showing the temperature distribution profile for E-BN25P, E-BN25, and E-BN25C without/with the cooling liquids; also see the modeling details and simulation results of the surface temperature of different layered microchannels in Fig. S19 & Tables S4-S5.

Supplementary Files

This is a list of supplementary files associated with this preprint. Click to download.

SpringerSupportingInfo.docx